Technische Universität Graz

Multi-objective free-form shape optimization of a synchronous reluctance machine

P. Gangl, S. Köthe, C. Mellak, A. Cesarano. A. Mütze

Berichte aus dem Institut für Angewandte Mathematik

Bericht 2020/12

Technische Universität Graz

Multi-objective free-form shape optimization of a synchronous reluctance machine

P. Gangl, S. Köthe, C. Mellak, A. Cesarano. A. Mütze

Berichte aus dem Institut für Angewandte Mathematik

Bericht 2020/12

Technische Universität Graz
Institut für Angewandte Mathematik
Steyrergasse 30
A 8010 Graz

WWW: `http://www.applied.math.tugraz.at`

Multi-objective free-form shape optimization of a synchronous reluctance machine

P. Gangl*, S. Köthe*, C. Mellak†, A. Cesarano*, and A. Mütze†

*Institute of Applied Mathematics, TU Graz, Steyrergasse 30, A-8010 Graz
† Electric Drives and Machines Institute, TU Graz, Inffeldgasse 18, A-8010 Graz
E-mail: gangl@math.tugraz.at

***Abstract*—This paper deals with the design optimization of a synchronous reluctance machine to be used in an X-ray tube, where the goal is to maximize the torque, by means of gradient-based free-form shape optimization. The presented approach is based on the mathematical concept of shape derivatives and allows to obtain new motor designs without the need to introduce a geometric parametrization. We validate our results by comparing them to a parametric geometry optimization in JMAG by means of a stochastic optimization algorithm. While the obtained designs are of similar shape, the computational time used by the gradient-based algorithm is in the order of minutes, compared to several hours taken by the stochastic optimization algorithm. Finally, we show an extension of the free-form shape optimization algorithm to the case of multiple objective functions and illustrate a way to obtain an approximate Pareto front.**

***Index Terms*—multiobjective shape optimization, shape derivative, synchronous reluctance machine.**

I. Introduction

In many industrial applications, the design of electric machines has to be tailored to the application at hand since off-the-shelf solutions are not available. The design of electric machines is usually based on engineering knowledge and is sometimes refined by geometric optimization. The most widely used approach is to introduce geometric parameters and optimize these, either using stochastic optimization algorithms or derivative-based methods, see [1] for an overview article. While derivative-based optimization algorithms successively improve a given initial geometry by means of gradient information and are known to converge to a local optimum rather fast, stochastic algorihtms include random effects and are less prone to getting stuck in local optima. In practice, one is usually confronted with several conflicting objective functions thus making multiobjective optimization capabilities for finding a Pareto optimal set of designs important. The extension to a multiobjective setting is more straightforward in the case of many stochastic optimization algorithms, however it can also be achieved in the case of derivative-based methods [2].

In recent years, non-parametric shape optimization methods based on the mathematical concept of shape derivatives [3] (often refered to free-form shape optimization approaches) have become a more and more popular tool for the design optimization of electric machines, see e.g. [4], [5], [6] for approaches using the finite element method or the recent work [7] in the context of isogeometric analysis. In these approaches, the geometry is not parametrized by a finite number of scalar values, but the design variable is a set, e.g. the set of points occupied by ferromagnetic material in the rotor of an electric machine. Starting out from a given initial design, the design is updated by the action of a smooth vector field, thus allowing for any kind of design that is topologically equivalent to the initial design. This way, often new and innovative designs can be obtained.

The purpose of this paper is two-fold: On the one hand, we extend the gradient-based multi-objective optimization method introduced in the case of a parametrized geometry in [2] to the case of free-form shape optimization. This allows to exploit the flexibility of free-form shape optimization methods, as well as their fast convergence properties also in the practically important case of multiple competing objective functions. On the other hand, we employ this method on both, the more standard single-objevtive case and, in the case of two objective functions, to find (Pareto-)optimal designs of a synchronous reluctance machine. Comparing our results with the results obtained by a stochastic parameter optimization confirms the higher degree of flexibility and computational efficiency of our approach compared to parametric design optimization.

The rest of this paper is organized as follows: In Section II we introduce the problem at hand and state the mathematical model. We recall the main ingredients for a free-form shape optimization method and apply the algorithm to our problem in Section III. In Section IV we show an extension of the gradient-based free-form shape optimization algorithm to the case of multiple objective functions before concluding in Section V.

II. Problem description

A. Physical model

We consider the design optimization of a synchronous reluctance machine (SynRM), i.e., a motor that is based solely on the reluctance principle. This motor generates torque exclusively by a difference of reluctance between two axes, namely the d-axis and the q-axis (the location of the axes is defined by the number of poles of the machine). Thus, torque generation is not based on any transient behavior or quantity and a static magnetic field analysis is sufficient. The machine under investigation

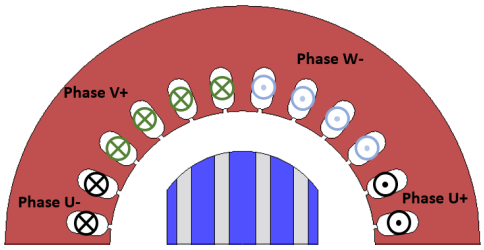

Figure 1. Upper half of synchronous reluctance machine with a three phase, two pole stator. The rotor consists of alternating magnetically conducting (blue) and non-conducting layers (gray).

Table I
EXAMPLE CASE MACHINE DESIGN PARAMETERS.

Parameter	Value
Stator	
Inner radius	26.5 mm
Outer radius	47.5 mm
Number of slots	24
Number of phases	3
Number of poles	2
Axial length	50 mm
Winding type	single-layer distributed
No. of turns per slot	64
Phase resistance $R_{\mathrm{S},20\,^\circ\mathrm{C}}$	7.1 Ω
Rated voltage U_{eff}	230 $\mathrm{V_{ac}}$/ 400 $\mathrm{V_{ac}}$
Connection	star
Rotor	
Outer radius	18.5 mm

is intended for the use in an X-Ray tube for medical applications. The considered rotor will be operated in a vacuum and therefore must be built of solid pieces of metal (as opposed to the commonly used steel sheet structure). Additionally, the air gap of the motor is unusually large (e.g., 10 mm with an outer stator diameter of 130 mm) decreasing the torque capability of the machine. Furthermore, the rotor has to withstand temperatures of up to 450 °C. [10]

The synchronous reluctance machine is particularly suitable for such an application mainly due to its ruggedness and construction simplicity and the absence of rotor windings [11]. As per the operation mode of the machine quick acceleration and subsequent braking of a tungsten disk is required. Typically, this sequence takes at maximum 10 s. Figure 1 shows the machine under investigation. The stator is a three phase stator with one pole pair, the rotor consists of alternating magnetically conducting (blue) and non-conducting layers (gray). The reference design parameters of the machine are stated in Table I.

Figure 2 shows the simplified vector diagram of a synchronous reluctance machine. The d-axis of the machine is the path with least reluctance, the q-axis is the path with the highest reluctance. In the d-q axis theory, the torque is expressed as

$$T = \frac{3N_p}{2}(\lambda_\mathrm{d}\mathrm{I_q} - \lambda_\mathrm{q}\mathrm{I_d}),$$

where N_p denotes the number of pole pairs, λ_d and λ_q are

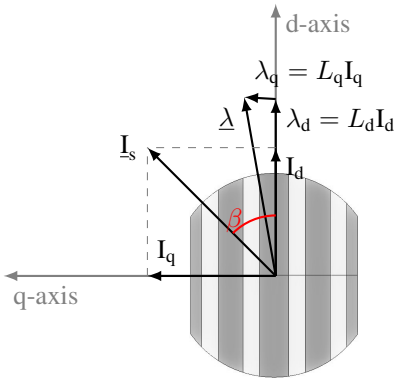

Figure 2. Vector diagram of a synchronous reluctance machine for the simplified model in d-q reference frame [9].

the magnetic flux linkages, and $\mathrm{I_d}$ and $\mathrm{I_q}$ are the currents in d-axis and q-axis direction, respectively. Alternatively, using the inductances L_d and L_q as well as the stator current $\mathrm{I_s}$ and current angle β, the torque is expressed as

$$T = \frac{3N_p}{4}(L_\mathrm{d} - L_\mathrm{q})\mathrm{I_s^2}\sin(2\beta)\,. \tag{1}$$

Evidently, as per (1), assuming linear lossless behaviour and a fixed stator current $\mathrm{I_s}$ the maximum torque can be achieved with a machine current angle β (angle between current vector and d-axis of the machine, Fig. 2) of 45°. [8]

B. Optimization goal

A static analysis is chosen to calculate the reluctance torque. Therefore, a current is impressed on the windings according to Table II. Subsequently, the rotor is rotated and fixed clockwise to create the optimal current angle β of 45°. The objective is to increase the torque with the given stator at a constant current and air gap length at the optimum current angle β. The number of conducting and non-conducting layers remains unchanged. Solely the shape of each individual layer is subject to the optimization as to increase the d-axis inductance L_d while, ideally, decreasing the q-axis inductance L_q at the same time.

Table II
THE CURRENT VALUES FOR EACH WINDING.

U-Phase	V-Phase	W-Phase
12 A	-6 A	-6 A

C. Mathematical model

We consider a two-dimensional cross-section of the machine in the setting of 2D magnetostatics, i.e., $\mathbf{B} = \mathrm{curl}\mathbf{A}$ where the magnetic vector potential is of the form $\mathbf{A} = (0, 0, u(x_1, x_2))^\top$. Let $D \subset \mathbb{R}^2$ denote the computational domain which comprises the two-dimensional cross section of the machine as well as a surrounding air

region, and let $\Omega \subset D$ denote the ferromagnetic parts of the machine. The mathematical design optimization problem reads

$$\max_{\Omega \in \mathcal{A}} T(u) \tag{2}$$

$$\begin{aligned} \text{s.t. } -\operatorname{div}(\nu_\Omega(x, |\nabla u|)\nabla u) &= J_i, \quad x \in D, \\ u &= 0, \quad x \in \partial D, \end{aligned} \tag{3}$$

where T represents the torque for the considered rotor position, $\mathcal{A}$ is a set of admissible shapes, J_i represents the impressed current density and the magnetic reluctivity is defined piecewise as

$$\nu_\Omega(x, s) = \begin{cases} \hat{\nu}(s) & x \in \Omega, \\ \nu_0 & x \in D \setminus \overline{\Omega}. \end{cases}$$

Here, $\hat{\nu}$ is a nonlinear function which represents the magnetic reluctivity of the ferromagnetic material, and ν_0 corresponds to the magnetic reluctivity of air. The partial differential equation (PDE) constraint (3) admits a unique solution under natural assumptions on the nonlinear function $\hat{\nu}$ [12]. Note that the torque T depends on the shape Ω of the ferromagnetic components via the solution to the PDE constraint (3). Denoting the unique solution to (3) for given $\Omega \in \mathcal{A}$ by u_Ω, we define the reduced cost function $\mathcal{T}(\Omega) := T(u_\Omega)$.

III. Free-form shape optimization

We propose a free-form shape optimization algorithm based on the mathematical concept of shape derivatives, which is capable of improving the shape of a given initial geometry without the need of defining geometric parameters. We will outline the main ingredients to the method in the following. We introduce the theory for a general cost function $\mathcal{J}$ and will choose $\mathcal{J} := -\mathcal{T}$ later in Section III-C.

A. Shape derivative

The shape derivative of a general shape function $\mathcal{J} = \mathcal{J}(\Omega)$ represents the sensitivity of $\mathcal{J}$ when the domain Ω is perturbed by the action of a given vector field V. Given a smooth vector field V which is defined on D, let $\Omega_t = (\mathrm{id} + tV)(\Omega)$ denote the perturbed domain for $t > 0$. The shape derivative of $\mathcal{J}$ in the direction given by V is defined as

$$d\mathcal{J}(\Omega; V) := \lim_{t \searrow 0} \frac{\mathcal{J}(\Omega_t) - \mathcal{J}(\Omega)}{t}, \tag{4}$$

provided that this limit exists and the mapping $V \mapsto d\mathcal{J}(\Omega; V)$ is linear and continuous [3].

The shape derivative for problem (2)–(3) can be derived in an analogous way as it was done in [4] and, for a vector field V that is only supported on the rotor, reads

$$\begin{aligned} d\mathcal{J}(\Omega; V) = \\ + \int_D \nu_\Omega(x, |\nabla u|) \left((\operatorname{div} V) I - \partial V^T - \partial V \right) \nabla u \cdot \nabla p \, \mathrm{d}x \\ - \int_D \frac{\partial_s \nu_\Omega(x, |\nabla u|)}{|\nabla u|} (\partial V^T \nabla u \cdot \nabla u)(\nabla u \cdot \nabla p) \, \mathrm{d}x. \end{aligned} \tag{5}$$

Here, p denotes the solution to the adjoint equation which for the case of the maximization of the torque reads in its strong form

$$\begin{aligned} \text{s.t. } -\operatorname{div}(A_\Omega(u)\nabla p) &= \frac{\partial T}{\partial u}, \quad x \in D, \\ p &= 0, \quad x \in \partial D. \end{aligned} \tag{6}$$

with

$$A_\Omega(u) := \nu_\Omega(x, |\nabla u|) I + \frac{\nu_\Omega'(x, |\nabla u|)}{|\nabla u|} \nabla u \otimes \nabla u.$$

B. Descent direction

Given a closed formula for the shape derivative, a descent vector field V can be obtained by solving an auxiliary boundary value problem as follows. Let X be a Hilbert space and $b : X \times X \to \mathbb{R}$ a symmetric and positive definite bilinear form. Then the solution $W \in X$ to the variational problem

$$b(W, V) = -d\mathcal{J}(\Omega; V) \; \forall V \in X \tag{7}$$

is a descent direction since it satisfies by construction

$$d\mathcal{J}(\Omega; W) = -b(W, W) < 0.$$

Thus, it follows from the definition in (4) that perturbing Ω a small distance into the direction W will yield a decrease of the cost function $\mathcal{J}$.

The user has some degrees of freedom in the choice of the bilinear form $b(\cdot, \cdot)$ as well as the space X. Common choices include $X = H^1(D, \mathbb{R}^2)$ and $b(W, V) = \int_D \partial W : \partial V + W \cdot V \mathrm{d}x$ or $b(W, V) = \int_D C\epsilon(W) : \epsilon(V) + W \cdot V \mathrm{d}x$ where $\epsilon(V) = \frac{1}{2}(\partial V + \partial V^\top)$ and C is a fourth-order elasticity tensor. The latter choice is known to preserve mesh quality better compared to other choices of $b(\cdot, \cdot)$ [13]. An alternative strategy for extracting a descent direction which also allows for the extension to multiple objective functions will be discussed in Section IV-A.

C. Numerical results

The procedure outlined in Sections III-A and III-B constitutes the following free-form shape optimization algorithm for minimization of shape function $\mathcal{J} = \mathcal{J}(\Omega)$:

Algorithm 1. *Given initial design Ω_0, cost function $\mathcal{J}$, tolerance tol, $k = 0$.*

1) *Solve state equation* (3) *and adjoint equation* (6)
2) *Compute shape derivative $d\mathcal{J}(\Omega_k; V)$ given in* (5)
3) *Compute shape gradient W as solution to* (7)
4) *If $\|W\| < tol$ then stop*
   else set $\Omega_{k+1} = (id + tW)(\Omega_k)$ where $t = max\{1, \frac{1}{2}, \frac{1}{4}, \frac{1}{8}, \dots\}$ such that $\mathcal{J}(\Omega_{k+1}) < \mathcal{J}(\Omega_k)$.
5) *$k \leftarrow k + 1$ and go back to 1)*

In step 4) the parameter t is chosen by a line search in order to guarantee a descent of the cost function $\mathcal{J}$.

We applied Algorithm 1 to problem (2)–(3), i.e. we chose to minimize $\mathcal{J}(\Omega) := -\mathcal{T}(\Omega)$, using the finite

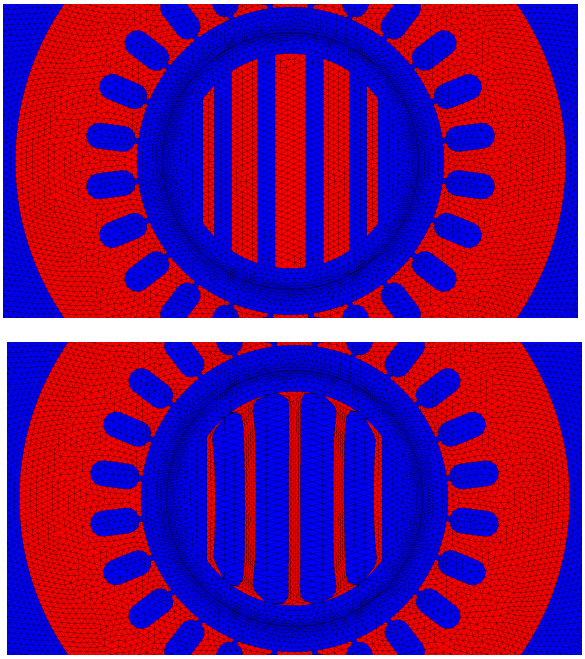

Figure 3. Top: Initial design of rotor, $T = 1.007$ Nm. Bottom: Optimized design obtained after 70 iterations of Algorithm 1, $T = 1.270$ Nm.

element software package NGSolve [14]. In particular, we used the automated shape differentiation capabilities provided by NGSolve which enables the automated computation of the shape derivative $d\mathcal{J}(\Omega; V)$ for a large class of PDE-constrained shape optimization problems [15].

For the space X in (7), we chose the space of all vector-valued H^1 functions defined on the rotor of the machine whose normal component vanishes on the top and bottom boundary parts of the rotor and which vanish at the left and right boundary parts. For the bilinear form $b(\cdot, \cdot)$ we chose the H^1 inner product

$$b(V, W) := \int_{D_{rot}} \partial V : \partial W + \frac{1}{100} V \cdot W \, \mathrm{d}x,$$

where D_{rot} denotes the union of the five iron and four air layers as depicted in Figure 3. The results obtained after 70 iterations of Algorithm 1 are depicted in Figure 3. The torque was increased by about 26% from 1.007 Nm to 1.270 Nm. The computational time to obtain the optimized design was about 10 minutes on a single core.

D. Validation

In this section, we validate the results obtained in our numerical experiments by comparing them to an optimization run in JMAG [16]. Motivated by the results of the gradient-based optimization, see Fig. 3, we parametrized our rotor geometry by means of 14 geometric parameters under symmetry conditions, see Fig. 4, and ran a genetic algorithm which is built into JMAG to maximize the torque. We started with a population size of 300 and ran the algorithm for 50 generations, allowing

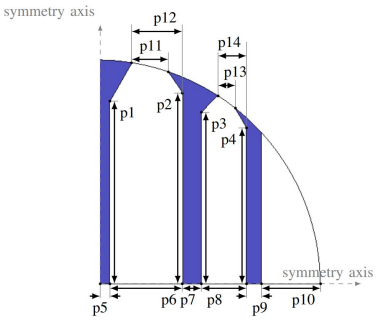

Figure 4. Geometric parameters used for genetic algorithm.

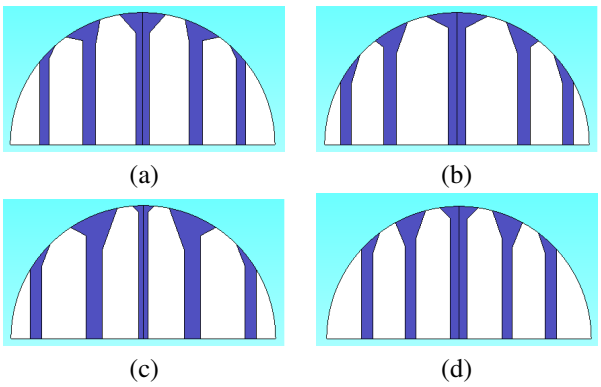

Figure 5. Best results obtained by genetic algorithm in JMAG based on geometric parametrization of Fig. 4 after 300 generations. (a) best design, $T = 1.2119$Nm. (b) second best design, $T = 1.2091$Nm. (c) third best design, $T = 1.2082$Nm. (d) fourth best design, $T = 1.2067$Nm.

for 60 children in each generation. The computational time used by the genetic algorithm was about 19 hours and a total of 15000 designs were examined. The four designs with the highest torque values are depicted in Fig. 5. It can be seen that the best designs are similar to the design we obtained by the gradient-based algorithm (Fig. 3), but also that the torque values were not quite reached. While one might be tempted to explain such a discrepancy by the fact that different simulation tools were used, we mention that the calculated torques in the two simulation softwares (NGSolve and JMAG) showed a good match for the initial geometry. Thus, it seems like the design in Fig. 3 is superior to those obtained by the genetic algorithm in JMAG since more general geometries can be obtained. Of course, the computation time of 19 hours could be reduced by reducing the parameters of the genetic algorithm, however the general order of magnitude remains. Finally note that, since the choice of the geometric parameters was inspired by Fig. 3, the designs in Fig. 5 would have been unlikely to be found without the knowledge provided by the free-form shape optimization algorithm.

IV. Multi-objective shape optimization

In this section we consider an extension of the gradient-based free-form shape optimization method presented in Section III to the setting of multiple objective

functions. We show how to compute a descent vector field W that assures a descent with respect to several objective functions and use this approach in order to obtain an approximation of the Pareto front. We apply the method to the bi-objective free-form shape optimization problem

$$\min_{\Omega} \begin{pmatrix} \mathcal{J}_1(\Omega) \\ \mathcal{J}_2(\Omega) \end{pmatrix}$$

where $\mathcal{J}_1(\Omega) := -\mathcal{T}(\Omega)$ corresponds to the negative of the torque related to Ω and $\mathcal{J}_2(\Omega) := \mathrm{Vol}(\Omega)$ denotes the volume of the ferromagnetic subdomains of the machine.

A. Multi-objective descent direction

Given two shape functions $\mathcal{J}_1$, $\mathcal{J}_2$ and their corresponding shape derivatives $d\mathcal{J}_i(\Omega; V)$, $i = 1, 2$, we want to find a vector field W such that

$$d\mathcal{J}_1(\Omega; W) < 0 \quad \text{and} \quad d\mathcal{J}_2(\Omega; W) < 0.$$

We extend the ideas introduced in the framework of parametric shape optimization in [2] to the setting of free-form shape optimization. For that purpose, we consider a finite element discretization using piecewise linear and globally continuous finite elements on a triangular mesh. Denoting the corresponding hat basis functions by $\varphi_1, \ldots, \varphi_n$ where n is the number of mesh points and $\Phi_i = (\varphi_i, 0)^\top$, and $\Phi_{n+i} = (0, \varphi_i)^\top$, $i = 1, \ldots, n$, we have that

$$\{\Phi_1, \ldots, \Phi_{2n}\}$$

is a basis for the set of all two-dimensional vector fields on the mesh. Thus, after discretization each vector field W_h can be written as $W_h = \sum_{i=1}^{2n} W_i \Phi_i$ with the coefficient vector $\underline{W} := (W_1, \ldots W_{2n})^\top$. Note that we can identify the finite element function W_h with its coefficient vector $\underline{W}$. In order to obtain a discrete bi-descent direction W_h, we solve the auxiliary optimization problem to find $(\rho, \underline{W}) \in \mathbb{R} \times \mathbb{R}^{2n}$

$$\begin{aligned} \min_{\rho, \underline{W}} \ & \rho + \frac{1}{2} \sum_{i=1}^{2n} W_i^2, \\ \text{s.t.} \quad & d\mathcal{J}_1(\Omega; W_h) \leq \rho, \\ & d\mathcal{J}_2(\Omega; W_h) \leq \rho. \end{aligned} \tag{8}$$

Due to the linearity of the shape derivatives $d\mathcal{J}_i(\Omega; W_h)$ with respect to W_h, the solution $(\rho, \underline{W}) = (0, \mathbf{0}) \in \mathbb{R} \times \mathbb{R}^{2n}$ is a feasible point of (8). Therefore, it follows that the solution $(\rho, \underline{W})$ to (8) satisfies $d\mathcal{J}_i(\Omega; W_h) \leq \rho \leq 0$, $i = 1, 2$, thus giving a bi-descent direction W_h whenever the optimal ρ is negative. The second term in the cost function of (8) is meant to keep the norm of W_h bounded.

We remark that, in contrast to the widely used weighted-sum method, this approach is also feasible for finding non-convex parts of a Pareto front [2]. Of course, an extension of this approach to account for more than two cost functions $\mathcal{J}_1, \ldots, \mathcal{J}_N$ is straightforward.

B. Obtaining a Pareto front

Proceeding as described in Section IV-A allows to obtain a bi-descent direction W_h. Thus, starting out from an initial design, iteratively computing a bi-descent vector field and moving the interface a small distance in the direction given by this vector field constitutes a gradient-based free-form shape optimization algorithm for two cost functions. When no further decrease can be obtained, a Pareto optimal point is found.

In order to obtain many Pareto optimal points, one could start with many different initial designs. However, it turns out to be more convenient to proceed as follows: Consider different scalings of the two objective functions, i.e. apply the gradient-based biobjective descent algorithm for the two objective functions $\mathcal{J}_1$ and $w\mathcal{J}_2$ with different values of the weight w, see also [2]. Each choice of the weight w corresponds to a run of the bi-objective descent algorithm and will yield a point on the Pareto front.

C. Numerical results

The proposed algorithm to obtain an approximation of a Pareto front consists in a loop over different weights w where each iteration uses an algorithm similar to Algorithm 1 to obtain an optimized design. In contrast to Algorithm 1, however, here the descent direction is obtained by solving the auxiliary optimization problem (8) rather than an auxiliary boundary value problem of the form (7). The algorithm reads as follows:

Algorithm 2. *Given initial design Ω_0, cost functions $\mathcal{J}_1, \mathcal{J}_2$, tolerance tol, set of weights $\{w_1, \ldots, w_M\}$.*
For $j = 1, \ldots, M$:

1) *If $j > M$ then stop*
   else set $\tilde{\mathcal{J}}_1 \leftarrow \mathcal{J}_1$, $\tilde{\mathcal{J}}_2 \leftarrow w_j \mathcal{J}_2$.
2) *Set $k \leftarrow 0$, $\Omega_0^{(j)} \leftarrow \Omega_0$*
3) *For $k = 0, 1, 2, \ldots$*
   (i) *Solve state equation* (3) *and adjoint equation* (6)
   (ii) *Compute shape derivatives $d\tilde{\mathcal{J}}_1(\Omega_k^{(j)}; V)$, $d\tilde{\mathcal{J}}_2(\Omega_k^{(j)}; V)$*
   (iii) *Compute bi-objective descent direction W_h as solution to* (8) *with $d\tilde{\mathcal{J}}_1(\Omega_k^{(j)}; \cdot)$, $d\tilde{\mathcal{J}}_2(\Omega_k^{(j)}; \cdot)$*
   (iv) *If $\|W_h\| < tol$ then $j \leftarrow j + 1$ and go to 1) else set $\Omega_{k+1}^{(j)} = (id + tW_h)(\Omega_k^{(j)})$ where $t = max\{1, \frac{1}{2}, \frac{1}{4}, \frac{1}{8}, \ldots\}$ such that $\mathcal{J}_i(\Omega_{k+1}^{(j)}) < \mathcal{J}_i(\Omega_k^{(j)})$, $i = 1, 2$.*

In our implementation, we solved the quadratic optimization problem involving linear inequality constraints (8) by means of a sequential least squares programming optimization algorithm using the functionality `scipy.optimize(...)`. In order to reduce computation time, we restricted problem (8) to the degrees of freedom on the material interfaces which are subject to optimization and neglected the interior degrees of freedom. This is motivated by the fact that a movement

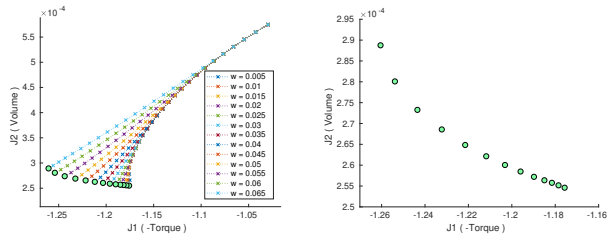

Figure 6. Left: Values of different designs obtained in the course of gradient based two-objective optimization algorithm for different weights w. Right: Zoom on approximated Pareto front.

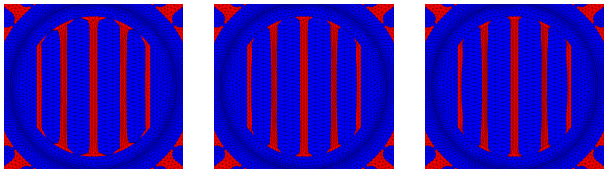

$w = 0.065$	$w = 0.035$	$w = 0.005$
$T = 1.260$	$T = 1.203$	$T = 1.176$
$V = 2.89 \cdot 10^{-4}$	$V = 2.60 \cdot 10^{-4}$	$V = 2.55 \cdot 10^{-4}$

Figure 7. Three different designs obtained on the approximated Pareto front by using different weights w for $\mathcal{J}_2$.

of points inside a subdomain does not alter the shape. Proceeding like this, we obtain a deformation vector field that is only supported on the material interfaces and vanishes on all interior mesh nodes. In order to avoid intersection of the mesh when updating the geometry, we extend the vector field from the interfaces to the whole rotor domain by harmonic extension, i.e., by solving an elliptic PDE. As additional constraints, we imposed the linear equality constraints that the normal component of the vector field on the boundary on the rotor domain vanishes, i.e. $W_x(z)n_x(z) + W_y(z)n_y(z) = 0$ for all mesh points $z \in \partial D_{rot}$. These constraints ensure that the radius of the rotor remains unchanged.

Figure 6 (left) shows the results of the bi-objective descent algorithm for minimizing the negative torque and w times the volume, $\mathcal{J}_1(\Omega) = -\mathcal{T}(\Omega)$ and $w\mathcal{J}_2(\Omega) = w\mathrm{Vol}(\Omega)$, for different choices of the weighting factor w. The right picture of Figure 6 depicts a zoom on the obtained Pareto optimal points. The computational effort for obtaining one Pareto optimal design is comparable to the cost of one single-objective optimization run (see Sec. III-C), amounting to a computational time of about two hours on a single core to obtain the depicted Pareto front. The Pareto optimal designs corresponding to three different choices of w can be seen in Figure 7.

V. Conclusion and Outlook

We addressed the problem of finding the optimal shape of the rotor of a synchronous reluctance machine as used in an X-ray tube by means of a gradient-based free-form shape optimization method which is based on the shape derivative. This approach allowed to obtain an optimized shape which exhibits an increase of the torque by 26% within only several minutes of computation time. The results are confirmed by a geometric parameter optimization in JMAG where the parametrization is motivated by the design obtained by free-form optimization. Moreover, we introduced an extension to the setting of multi-objective shape optimization and showed a way to obtain an approximate Pareto front while significantly decreasing the computation time when compared to evolutionary algorithms.

In this paper we only considered shape optimization approaches which cannot alter the connectivity of the initial design. A next step would be to consider topology optimization methods to additionally allow for changing topologies, in particular in the context of multi-objective optimization. While this was beyond the scope of this paper, it is subject of future work.

Acknowledgments

Alessio Cesarano has been funded by the Austrian Science Fund (FWF) project P 32911.

References

[1] G. Bramerdorfer, J. Tapia, J. Pyrhönen and A. Cavagnino, "Modern Electrical Machine Design Optimization: Techniques, Trends, and Best Practices,", IEEE Trans. Ind. Electron., vol. 65, pp. 7672–7684, 2018.

[2] O. Doganay, H. Gottschalk, C. Hahn, K. Klamroth, J. Schultes, and M. Stiglmayr, "Gradient based biobjective shape optimization to improve reliability and cost of ceramic components", Optim. Eng., 2019.

[3] M. Delfour and J.-P. Zolésio, Shapes and geometries, 2nd ed., vol. 22. Advances in Design and Control (SIAM), Philadelphia, 2011.

[4] P. Gangl, U. Langer, A. Laurain, H. Meftahi, and K. Sturm, "Shape optimization of an electric motor subject to nonlinear magnetostatics", SIAM J. Scient. Comp., 37(6):B1002–B1025, 2015.

[5] E. Kuci, "Shape and topology optimization for electro-mechanical energy converters", Doctoral dissertation, Université de Liège, Liège, Belgium, 2018.

[6] P. Putek, R. Pulch, A. Bartel, E.J. ter Maten, M. Günther, and K. Gawrylczyk, "Shape and topology optimization of a permanent-magnet machine under uncertainties", J. Math. Industry vol. 6, 2016.

[7] M. Merkel, P. Gangl, and S. Schöps, "Shape Optimization of Rotating Electric Machines using Isogeometric Analysis and Harmonic Stator-Rotor Coupling", arXiv eprint 1908.06009, submitted for publication.

[8] C. Spargo, "Synchronous reluctance technology : part I." *MagNews.*, no. Winter, January 2013. [Online]. Available: http://dro.dur.ac.uk/18579/

[9] A. Binder, *Elektrische Maschinen und Antriebe*. Springer, 2012.

[10] C. Mellak, and K. Krischan and A. Muetze, "Synchronous Reluctance Machines as Drives for Rotary Anode X-Ray Tubes – A Feasibility Study", ICEM 2018, pp. 2613–2618, 2018.

[11] L. Xu, X. Xu, Xingyi, T. Lipo, and D. Novotny, "Vector control of a synchronous reluctance motor including saturation and iron loss", IEEE Trans. Ind. Appl., vol 27(5), pp.977–985, 1991.

[12] C. Pechstein and B. Jüttler, "Monotonicity-preserving interproximation of B-H-curves", J. Comp. App. Math., 196:45–57, 2006.

[13] J. A. Iglesias, K. Sturm, and F. Wechsung, "Two-dimensional shape optimization with nearly conformal transformations", SIAM J. Scient. Comp., 40(6):A3807–A3830, 2018.

[14] J. Schöberl, "C++11 implementation of finite elements in NGSolve", Technical Report 30, Institute for Analysis and Scientific Computing, Vienna University of Technology, 2014.

[15] P. Gangl, K. Sturm, M. Neunteufel, J. Schöberl, "Fully and Semi-Automated Shape Differentiation in NGSolve", Struct. Multidisc. Optim., accepted.

[16] JSOL-Corporation,"JMAG : Simulation Technology for Electromechanical Design", http://www.jmag-international.com/.

Erschienene Preprints ab Nummer 2018/3

2018/7	O. Steinbach, M. Zank: Coercive space-time finite element methods for initial boundary value problems
2018/8	S. Dohr, K. Niino, O. Steinbach: Space-time boundary element methods for the heat equation
2018/8	O. Steinbach, H. Yang: Space-time finite element methods for parabolic evolution equations: Discretization, a posteriori error estimation, adaptivity and solution
2019/1	O. Steinbach (eds.): 15th Austrian Numerical Analysis Day, Book of Abstracts
2019/2	P. Gangl, K. Sturm: A simplified derivation technique of topological derivatives for quasi-linear transmission problems
2019/3	M. Merkel, P. Gangl, S. Schöps: Shape Optimization of Rotating Electric Machines using Isogeometric Analysis and Harmonic Stator-Rotor Coupling
2019/4	P. Gangl and K. Sturm: Asymptotic analysis and topological derivative for 3D quasi-linear magnetostatics
2019/5	M. Holzmann and G. Unger: Boundary integral formulations of eigenvalue problems for elliptic differential operators with singular interactions and their numerical approximation by boundary element methods
2019/6	M. Neumüller, O. Steinbach: Regularization error estimates for distributed control problems in energy spaces
2019/7	U. Langer, M. Schanz, O. Steinbach, W. L. Wendland (eds.): 17th Workshop on Fast Boundary Element Methods in Industrial Applications , Book of Abstracts
2019/8	O. Steinbach, M. Zank: A note on the efficient evaluation of a modified Hilbert transformation
2019/9	P. Gangl: A multi-material topology optimization algorithm based on the topological derivative
2020/1	D. Pacheco, T. Müller, O. Steinbach, G. Brenn: A mixed finite element formulation for generalised Newtonian fluid flows with appropriate natural outflow boundary conditions
2020/2	U. Langer, O. Steinbach, F. Tröltzsch, H. Yang: Unstructured space-time finite element methods for optimal sparse control of parabolic equations
2020/3	D.R.Q. Pacheco, R. Schussnig, O. Steinbach, T.-P. Fries: A fully consistent equal-order finite element method for incompressible flow problems
2020/4	U. Langer, O. Steinbach, F. Tröltzsch, H. Yang: Unstructured space-time finite element methods for optimal control of parabolic equations
2020/5	P. Gangl, K. Sturm, M. Neunteufel, J. Schöberl: Fully and Semi-Automated Shape Differentiation in NGSolve
2020/6	U. Langer, O. Steinbach, F. Tröltzsch, H. Yang: Space-time finite element discretization of parabolic optimal control problems with energy regularization
2020/7	G. Of, R. Watschinger: Complexity analysis of a fast directional matrix-vector multiplication
2020/8	P. Gangl, K. Sturm: Topological derivative for PDEs on surfaces
2020/9	D. R. Q. Pacheco, O. Steinbach: A continuous finite element framework for the pressure Poisson equation allowing non-Newtonian and compressible flow behaviour
2020/10	S. Kurz, S. Schöps, G. Unger, F. Wolf: Solving Maxwell's Eigenvalue Problem via Isogeometric Boundary Elements and a Contour Integral Method
2020/11	U. Langer, M. Schanz, O. Steinbach, W. L. Wendland (eds.): 18th Workshop on Fast Boundary Element Methods in Industrial Applications , Book of Abstracts